NANO LETTERS

pubs.acs.org/NanoLett Letter

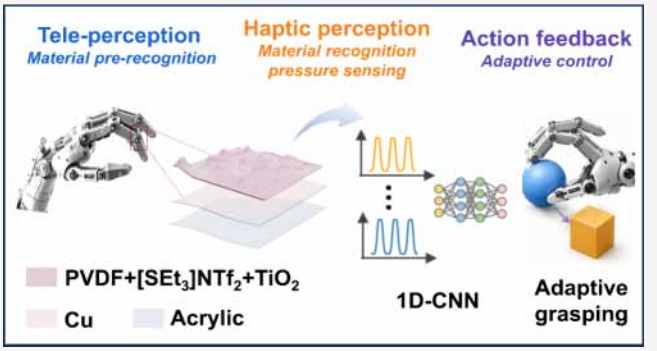
Iontronic Triboelectric Sensing for Adaptive Robotic Perception before and during Contact

Jiaxin Guo,[#] Yan Du,[#] Zhong Lin Wang,[*] and Di Wei[*]

Cite This: *Nano Lett.* 2026, 26, 13053−13062 Read Online

ACCESS | Metrics & More | Article Recommendations | Supporting Information

ABSTRACT: Adaptive robotic manipulation requires sensing systems capable of both anticipating contact and resolving haptic interactions. Existing triboelectric sensors operate through electron transport alone and are intrinsically limited to contact-triggered signal generation, preventing unified tele-perception and haptic perception. Here we introduce an iontronic triboelectric sensor (ITS) that exploits coupled ionic and electronic carrier transport to stabilize triboelectric charge generation while extending electrostatic perception beyond physical contact. Based on a PVDF-ionic liquid-TiO_2 composite dielectric with optimized surface microstructuring, the ITS enables haptic pressure sensing over 0−70 kPa in the contact-separation mode and human-target tele-perception up to 1.1 m in the single-electrode mode. The same 1D-CNN is independently applied, achieving 91.3% accuracy for material pre-recognition before contact and 90.28% accuracy for material recognition during contact. Integrated with a robotic hand, the ITS enables closed-loop tele-perception−haptic perception−action feedback for adaptive grasping, providing a self-powered multimodal platform for embodied intelligence and autonomous robotics.



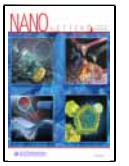
KEYWORDS: *Iontronic triboelectric sensing, triboelectric nanogenerators, haptic perception, tele-perception*

Embodied intelligence is reshaping robotics from executing predefined tasks to autonomously interacting with dynamic, unstructured environments. Such capability critically depends on adaptive perception that allows robots to recognize surrounding objects before physical contact while simultaneously acquiring rich haptic information during manipulation.[1−3] Existing sensing technologies, however, largely separate these two complementary functions. Conventional contact-dependent haptic sensors, including force/torque,[4,5] piezoresistive[6,7] or piezoelectric,[8,9] and capacitive variants,[10,11] provide accurate mechanical feedback during physical interaction. In contrast, non-contact approaches, including optical,[12,13] acoustic,[14] and magnetic sensing,[15,16] enable pre-contact perception and proactive environmental awareness. However, these complementary functions are generally realized through separate sensing mechanisms and platforms, often involving additional system complexity or continuous power requirements.[17,18] Integrating tele-perception and haptic perception within a unified self-powered sensing platform therefore remains a central challenge for adaptive robotic manipulation and intelligent human−machine interaction.

Triboelectric sensing based on triboelectric nanogenerators (TENGs) is promising for self-powered robotic perception owing to its high sensitivity, mechanical flexibility, and simple architecture.[19−21] Material and structural engineering, including porous elastomeric architectures and high-dielectric polymer nanocomposites, can markedly enhance triboelectric charge generation and energy conversion.[22−24] Beyond energy harvesting, triboelectric sensors have recently demonstrated the capability for electrostatic tele-perception, revealing the possibility of integrating remote object recognition with haptic sensing.[25−27] However, despite substantial advances in materials engineering[28,29] and structural design,[30−32] triboelectric sensors remain fundamentally limited by electron-only charge transport. Electron-cloud-dominated polarization constrains dielectric permittivity, surface charge density, and charge retention,[33,34] causing output degradation during prolonged operation and at increasing sensing distances. Overcoming these intrinsic limitations requires a transition from purely electronic charge transport to a fundamentally new triboelectric-sensing mechanism.

Iontronics offers an emerging strategy to transcend the limitations of conventional electronic dielectric systems by introducing mobile ionic carriers into charge transport. Ionic polarization can produce substantially stronger dielectric responses than conventional electronic polarization by

Received: July 13, 2026
Revised: September 8, 2026
Accepted: September 9, 2026
Published: September 17, 2026



ACS Publications © 2026 American Chemical Society

https://doi.org/10.1021/acs.nanolett.6c03434
Nano Lett. 2026, 26, 13053−13062

Downloaded from pubs.acs.org/naletd/article-pdf/26/38/13053/6854065/acs.nanolett.6c03434.pdf by BEIJING INST PETROCHEMICAL TECHLGY user on 01 October 2026

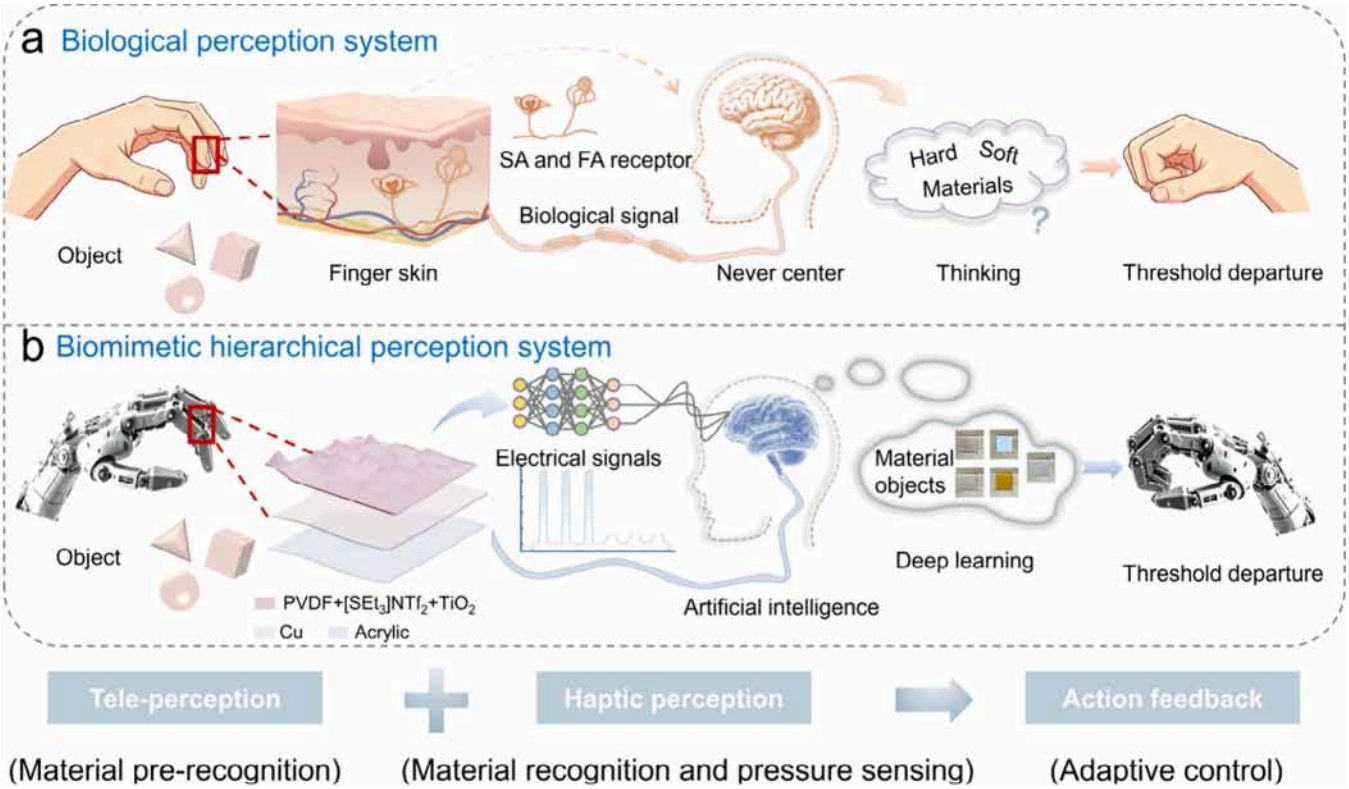


Figure 1. Working principle and design concept of the biomimetic bimodal perception system. (a) Schematic of the human biological perception system. (b) The biomimetic bimodal perception system integrating tele-perception with haptic perception.

exploiting ion migration and electrical double layer (EDL) formation,[35−38] whereas semiconductor nanomaterials with abundant deep trapping states suppress charge dissipation by stabilizing localized charges.[39−41] These strategies, however, have been largely developed independently. Triboelectric sensing has been enhanced either through ionic media, including hydrogels,[42,43] ionogels,[44,45] or liquid−solid interfaces,[46−48] or through deep-trap engineering to improve charge retention. Their synergistic integration has remained largely unexplored. Ionic polarization alone may suffer from uncontrolled ion migration and unstable charge retention, whereas deep-trap engineering cannot overcome the weak dielectric polarization of electron-only systems and may suffer from poor polymer compatibility.[49−51] Establishing a synergistic ionic-electronic charge transport mechanism that simultaneously promotes dielectric polarization and stabilizes triboelectric charges therefore represents a critical yet largely unexplored opportunity for advancing triboelectric sensing.

Herein, we introduce an iontronic triboelectric sensor (ITS) based on an engineered poly(vinylidene fluoride) (PVDF)-ionic liquid (IL)-TiO_2 composite dielectric that establishes synergistic ionic-electronic charge transport. IL-mediated interfacial polarization reconstructs the EDL to enhance dielectric polarization, whereas TiO_2-assisted charge trapping suppresses charge dissipation. Unlike conventional electron-only systems, this coupled transport enables stable tele-perception and haptic perception within a single platform. Combined with optimized surface microstructuring, the ITS achieves haptic sensing over 0−70 kPa in the contact-separation mode, while enabling meter-scale human-target detection up to 1.1 m in the single-electrode tele-perception mode. The same one-dimensional convolutional neural network (1D-CNN) achieves 91.3% accuracy for material prerecognition before contact and 90.28% for material recognition during contact. Furthermore, the ITS enables a closed-loop robotic manipulation framework that converts multimodal sensory information to proactive grasping decisions. This work expands triboelectric sensing from a contact-triggered electronic platform to an integrated iontronic perception system, establishing a versatile sensing paradigm for embodied intelligence, autonomous robotics, and next-generation human−machine interaction.

Human skin perceives mechanical stimuli through cutaneous mechanoreceptors, which transduce mechanical deformation into biological signals for neural processing and material recognition (Figure 1a). This haptic perception enables discrimination of surface and mechanical properties but requires a direct physical contact. To overcome this limitation while retaining the biological principle of haptic perception, we developed a biomimetic bimodal perception system centered on the ITS (Figure 1b) by integrating an engineered tele-perception modality with conventional haptic perception, the proposed system extends haptic sensing beyond physical contact, enabling seamless perception both prior to and during contact within a unified sensing framework.

The system employs a PVDF-IL-TiO_2 ternary composite film as the core dielectric layer, with fabrication details provided in the article and in Figure S1. Before contact, electrostatic induction generates electrical signals for tele-perception to material prerecognition. Upon contact, the ITS provides haptic signals for the material recognition and pressure sensing. Signals from both stages were independently analyzed using the same 1D-CNN architecture. Supported by a closed-loop feedback architecture, the system continuously

https://doi.org/10.1021/acs.nanolett.6c03434
Nano Lett. 2026, 26, 13053−13062

Downloaded from pubs.acs.org/naletd/article-pdf/26/38/13053/6854065/acs.nanolett.6c03434.pdf by BEIJING INST PETROCHEMICAL TECHLGY user on 01 October 2026

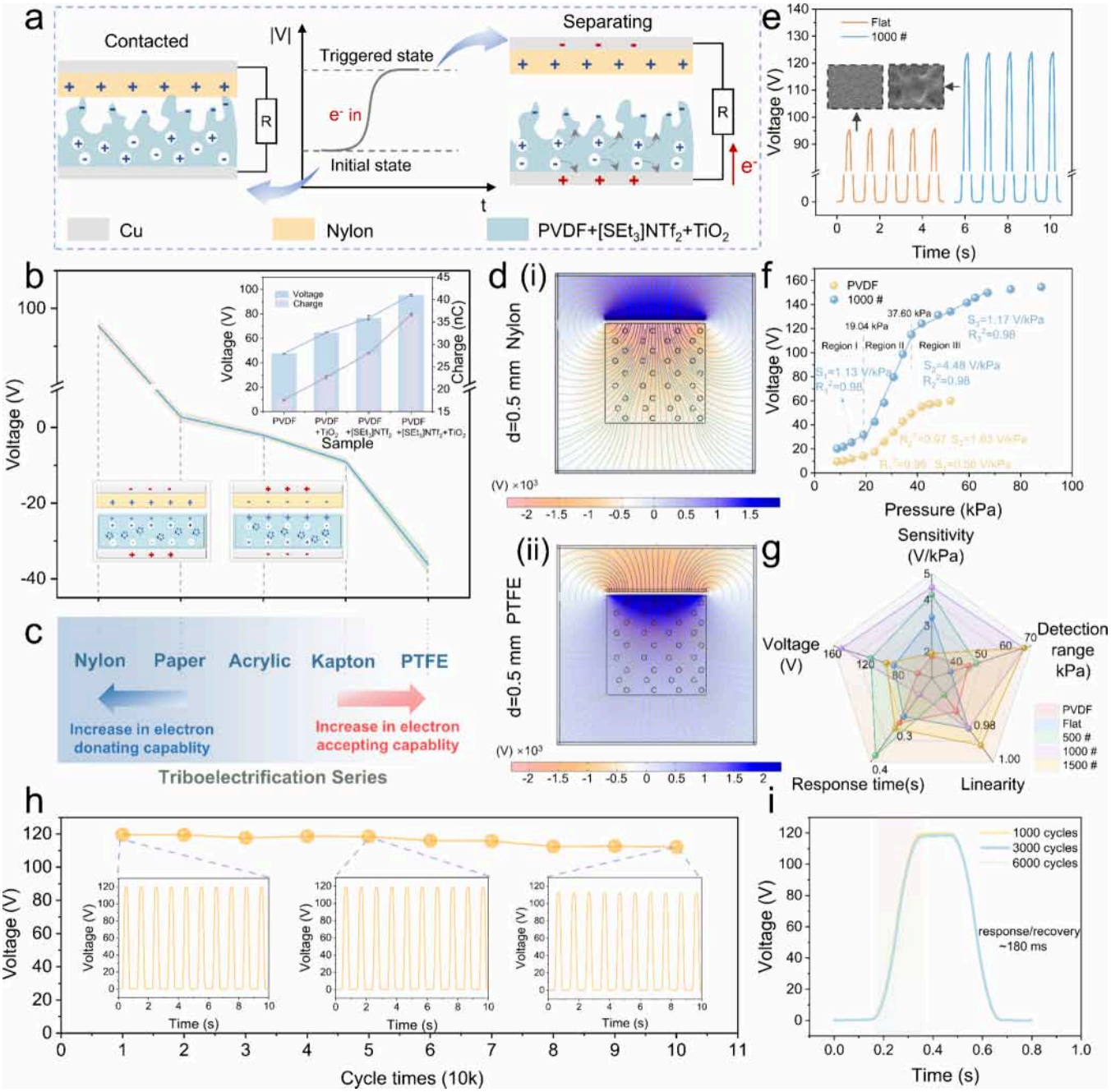


Figure 2. Mechanism and performance of haptic perception. (a) Schematic illustration of the contact-separation mode for haptic perception. (b) Adaptability of the ITS to various contacting materials. Inset shows the open-circuit voltage and transferred charge of different dielectric layers with nylon as the approach object. (c) Triboelectric series of the selected materials. (d) Finite element simulation (COMSOL) of the surface potential distribution upon contact with nylon and PTFE. (e) Comparison of output performance between flat and microstructured (1000#) surfaces of the optimized composite. (f) Pressure-dependent voltage responses of pristine PVDF and the 1000# microstructured ITS. The 1000# ITS exhibits three linear regimes (8.80−19.04, 19.04−37.60, and 37.60−67.20 kPa) with sensitivities of 1.13, 4.48, and 1.17 V kPa^{-1}, respectively; dashed lines mark the regime boundaries. (g) Radar-chart comparison of output voltage, pressure range, sensitivity, linearity, and response time for pristine PVDF and the flat, 500#, 1000#, and 1500# microstructured composite devices. (h) Cyclic stability test under a 1 Hz excitation frequency over 100000 cycles. (i) Dynamic response characteristics of the ITS, showing a response time and recovery time of approximately 180 ms.

monitors the contact pressure and automatically adjusts the grasping behavior once the output voltage exceeds a predefined threshold.

As illustrated in Figure 2, the ITS operates in the contact-separation mode for haptic perception through ionic-electronic coupling, with charge transfer proceeding through four stages (Figure S2). (I) Initial contact: according to the triboelectric series, nylon acts as the electron donor, becoming positively charged while the composite film acquires negative triboelectric charges. At this stage, the IL remains homogeneously distributed within the PVDF matrix with negligible ionic redistribution. (II) Separation: as the surfaces separate, electrostatic induction establishes a potential difference that drives electron flow through the external circuit. Meanwhile, the resulting internal electric field induces ion migration and space-charge formation within the composite, enhancing

https://doi.org/10.1021/acs.nanolett.6c03434
Nano Lett. 2026, 26, 13053−13062

Downloaded from pubs.acs.org/naletd/article-pdf/26/38/13053/6854065/acs.nanolett.6c03434.pdf by BEIJING INST PETROCHEMICAL TECHLGY user on 01 October 2026

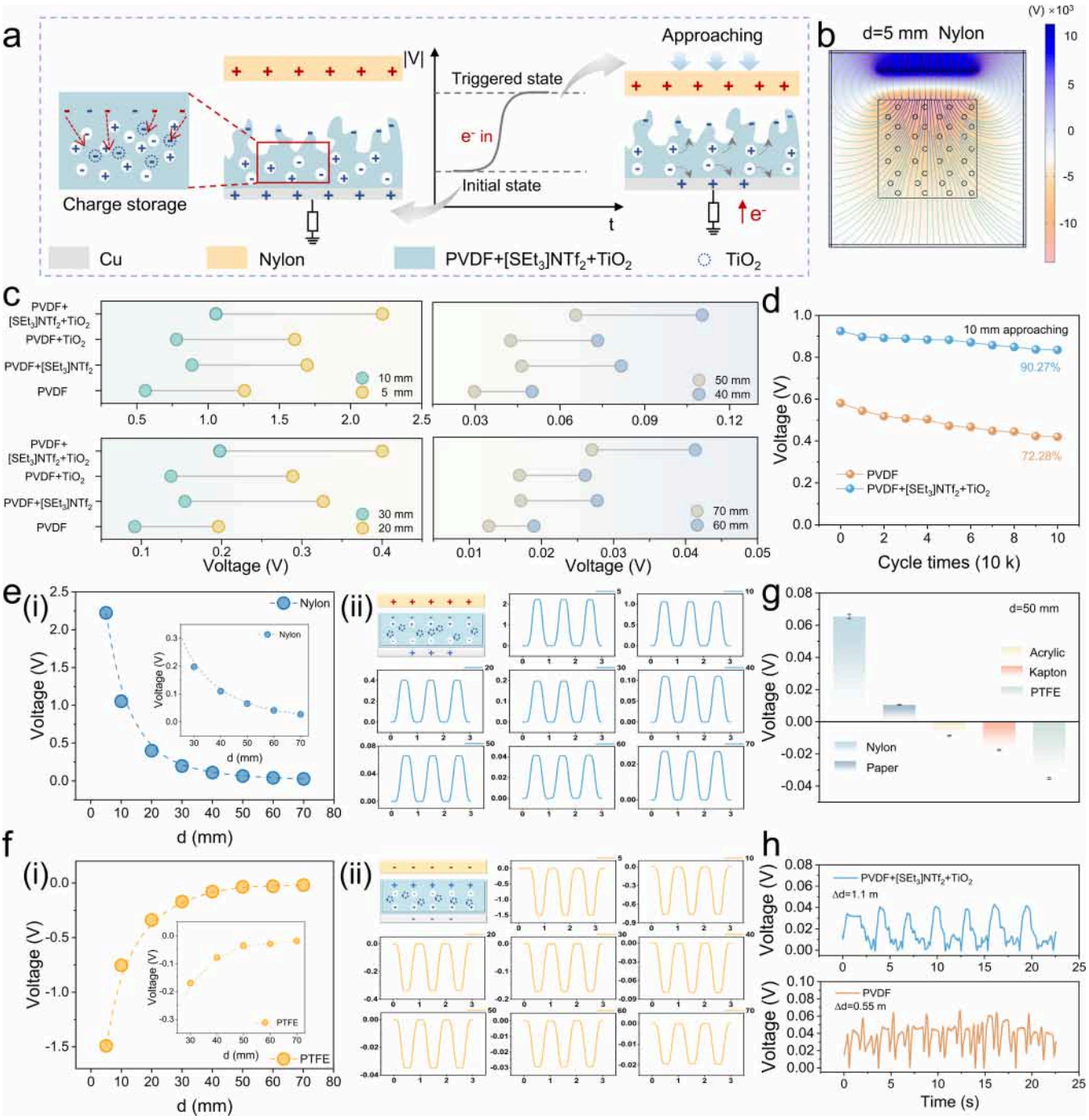


Figure 3. Mechanism and performance of tele-perception. (a) Schematic illustration of the single-electrode mode for tele-perception. (b) Finite element simulation (COMSOL) of the surface potential when a nylon approaches a distance of 5 mm. (c) The output voltage of different dielectric layers as a function of distance (0-70 mm) with nylon as the approaching object. (d) Cyclic stability test in the single-electrode tele-perception mode over 100,000 repeated approach-retraction cycles at 1 Hz, with a minimum sensor-target separation of 10 mm. (e, f) Dynamic sensing responses to positively charged nylon and negatively charged PTFE objects within a 0−70 mm range. (g) Quantitative comparison of ITS responses to five materials with distinct work functions at a fixed distance of 50 mm. (h) Tele-perception responses of the optimized ITS and pristine PVDF to an approaching human target at 25 °C and ∼38% RH, with the optimized ITS retaining ∼0.04 V at 1.1 m.

dielectric polarization. (III) Maximum separation: induced electrode charges compensate the triboelectric charges on nylon, while cations and anions accumulate at the polymer−air and polymer−Cu interfaces, respectively, forming EDLs that maximize interfacial capacitance and output voltage. (IV) Re-contact: the decreasing potential difference reverses electron flow until electrostatic equilibrium is restored, generating alternating electrical outputs during repeated contact-separation cycles. The composite exhibits a bulk ionic conductivity of $\sim 5.36 \times 10^{-6}$ S cm^{-1}, providing sufficient ionic mobility for internal charge redistribution and interfacial polarization (Figure S3). Together with homogeneous IL distribution, EDL formation enhances charge compensation while suppress-

https://doi.org/10.1021/acs.nanolett.6c03434
Nano Lett. 2026, 26, 13053−13062

Downloaded from pubs.acs.org/naletd/article-pdf/26/38/13053/6854065/acs.nanolett.6c03434.pdf by BEIJING INST PETROCHEMICAL TECHLGY user on 01 October 2026

ing premature neutralization, thereby improving dielectric polarization, charge retention, and electrical output.

To maximize energy conversion efficiency, the dielectric composite was systematically optimized by varying IL chemistry, IL loading, and TiO_2 content. All tests were performed on 2.5 × 2.5 cm^2 devices under contact-separation at 1 Hz with a 20 mm displacement. First, systematic screening of ILs and conductive salts (Figure S4a) revealed that $[SEt_3]NTf_2$ delivers the highest peak output voltage (~75 V), significantly outperforming the other tested electrolytes (LiTFSI and BMIMTFSI). Its moderate ion-pair binding energy facilitates ion diffusion and EDL formation, while relatively low bulk conductivity suppresses excessive back-charge migration and improves charge retention. $[SEt_3]NTf_2$ also increases the dielectric constant without pronounced charge screening (Figures S3 and S5), and XRD confirms enhanced electroactive β-phase formation after IL incorporation (Figure S6). Second, a PVDF:$[SEt_3]NTf_2$ mass ratio of 1:1 yielded the optimal performance (Figure S4b), balancing sufficient ion density for interfacial polarization against excessive ionic mobility, electrostatic screening, and charge leakage. Excessive IL loading promotes the formation of local ion-rich regions and enhances ionic mobility, facilitating internal charge redistribution and partial electrostatic screening, which can increase charge leakage and reduce the output. In contrast, insufficient IL content limits the available ion density for interfacial polarization, thereby weakening the triboelectric response. Finally, 2 wt % TiO_2 produced the highest output (Figure S4c), where TiO_2-assisted charge trapping synergized with IL-driven EDL formation to suppress charge recombination and improve charge retention. Surface-potential measurements confirmed this effect: the ternary composite retained 83.3% of its initial potential after 800 s, compared with 22.3% for pristine PVDF (Figure S7). However, higher TiO_2 contents caused nanoparticle aggregation and performance degradation. Thus, the optimal formulation was PVDF:$[SEt_3]NTf_2$ = 1:1 with 2 wt % TiO_2.

The electrical output of the optimized ITS was systematically evaluated (Figure 2b and Figure S8). The ternary composite exhibited a substantially higher surface charge density than pristine PVDF and the TiO_2-only system, supporting the synergistic effect of ionic migration and dielectric modulation. The triboelectric series (Figure 2c) places the composite between paper and acrylic. As the counter material changes from nylon to PTFE, increasing electron affinity produces a corresponding rise in open-circuit voltage, demonstrating broad material adaptability and enabling material-dependent signal differentiation. COMSOL simulations (Figure 2d) further reveal pronounced non-uniform electric-field distributions under contact with both nylon and PTFE. The resulting localized field intensification promotes efficient charge separation, thereby contributing to an enhanced output performance. Detailed simulation parameters, including the governing equation, material properties, boundary conditions, surface charge density settings, and mesh independence verification, are provided in Note S1 of the Supporting Information.

To further improve sensitivity, sandpaper-templated microstructures were introduced. The replicated friction layers closely preserved the template morphology, confirming high-fidelity structural transfer (Figure S9). To assess fabrication reproducibility, five independently selected sandpaper templates were used for each grit size (500#, 1000#, and 1500#). The resulting devices showed limited variation in open-circuit voltage, supporting the reproducibility of the templating process (Figure S10). The microtexturing increases the effective contact area and enhances interfacial charge generation, with the 1000# device exhibiting a markedly higher output than the flat control (Figure 2e). Under 1 Hz contact-separation with a 20 mm displacement, the 1000# microstructured ITS achieved a pressure sensing range up to 70 kPa (Figure 2f). Within the fitted range of 8.80−67.20 kPa, three piecewise-linear regimes were identified: 8.80−19.04 kPa with a sensitivity of 1.13 V kPa^{-1} (R^2 = 0.98), 19.04−37.60 kPa with 4.48 V kPa^{-1} (R^2 = 0.98), and 37.60−67.20 kPa with 1.17 V kPa^{-1} (R^2 = 0.98), with boundaries at 19.04 and 37.60 kPa. This three-stage response arises from progressive engagement of the replicated microstructures: At relatively low pressures, contact is mainly confined to the highest surface asperities, resulting in a gradual increase in the effective contact area. Above 19.04 kPa, progressive deformation and engagement of additional microstructures lead to a more rapid increase in the real contact area and interfacial triboelectric charge generation, accounting for the enhanced sensitivity in Region II. Beyond 37.60 kPa, the effective contact area progressively approaches saturation, such that further loading mainly compresses the established contact regions, resulting in the reduced sensitivity observed in Region III. Comparison of pristine PVDF, the flat composite, and the 500#, 1000#, and 1500# devices showed that the 1000# structure provided the best overall balance of output voltage, pressure detection range, sensitivity, linearity, and response time (Figure 2g), owing to its intermediate microstructural scale. The output remained above 90% of its initial value after 100,000 cycles (Figure 2h), and both response and recovery times were approximately 180 ms (Figure 2i), demonstrating robust and reproducible haptic sensing performance. Collectively, these results demonstrate that the ITS integrates high sensitivity, broad detection range, and robust long-term stability, providing a solid hardware foundation for haptic perception and closed-loop manipulation.

High ionic mobility within the IL enables rapid ionic relaxation and EDL formation under external electrostatic stimuli, enhancing the dielectric polarization and long-range electrostatic coupling. Concurrently, TiO_2 provides charge-trapping sites that immobilize charges and suppress the leakage within the dielectric matrix. Together with EDL-induced space-charge accumulation, this trap-assisted charge storage reduces charge dissipation and stabilizes long-range electrostatic signals, enabling tele-perception prior to physical contact. As illustrated in Figure 3a, an approaching positively charged object (e.g., nylon) redistributes negative charges within the composite, while ionic reorganization drives positive-charge accumulation on the Cu electrode and induces electron backflow to restore electrostatic equilibrium. A negatively charged object (e.g., PTFE) produces the opposite interfacial polarization and charge migration (Figure S12). COMSOL simulations (Figure 3b and Figure S13) further reveal distance-dependent potential evolution, confirming enhanced electric field modulation and long-range sensing stability.

To evaluate dielectric engineering, different dielectric configurations were compared using nylon as the target material (Figure 3c and Figure S14). The PVDF-$[SEt_3]NTf_2$-TiO_2 composite produced the highest output, reflecting the combined effects of ionic polarization and deep-trap-mediated charge stabilization. Cycling stability was further evaluated in

https://doi.org/10.1021/acs.nanolett.6c03434
Nano Lett. 2026, 26, 13053−13062

Downloaded from pubs.acs.org/naletd/article-pdf/26/38/13053/6854065/acs.nanolett.6c03434.pdf by BEIJING INST PETROCHEMICAL TECHLGY user on 01 October 2026

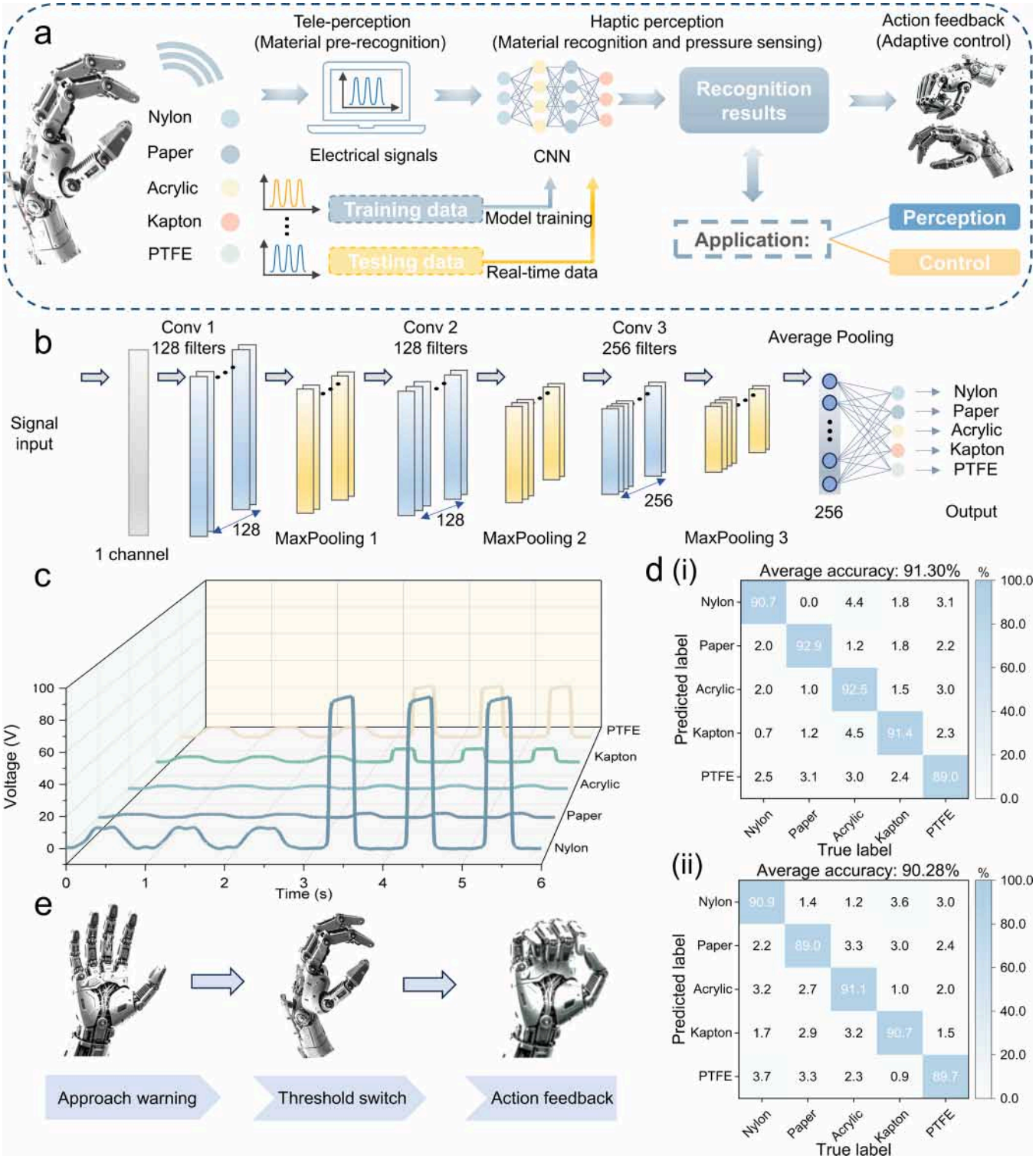


Figure 4. Biomimetic bimodal perception system for material recognition and human−machine interaction. (a) Schematic illustration of the working principle of the biomimetic bimodal perception system for material recognition and human−machine interaction. (b) Architecture and parameter configuration of the 1D-CNN used for signal processing. (c) Real-time voltage signals captured during the approach and contact phases for five representative materials. (d) Confusion matrices evaluating the material classification performance in (i) tele-perception mode using signals acquired at a fixed sensor-target separation of 50 mm and (ii) haptic perception mode under contact. (e) Schematic illustration of the closed-loop control strategy from sensing to action.

the single-electrode tele-perception mode at 1 Hz with a minimum sensor-target separation of 10 mm (Figure 3d). After 100,000 cycles, the ITS exhibited only 9.73% voltage decay, compared with 27.72% for pristine PVDF, confirming improved signal stability. Figure 3e and f shows distance-dependent tele-perception toward positively charged nylon and negatively charged PTFE over 0−70 mm. The output magnitude varies monotonically with distance, while signal

https://doi.org/10.1021/acs.nanolett.6c03434
Nano Lett. 2026, 26, 13053−13062

Downloaded from pubs.acs.org/naletd/article-pdf/26/38/13053/6854065/acs.nanolett.6c03434.pdf by BEIJING INST PETROCHEMICAL TECHLGY user on 01 October 2026

polarity identifies the charge sign of the approaching object. This polarity cue provides pre-contact information on target triboelectric characteristics, supporting material classification and subsequent adaptive grasp selection. At shorter distances, larger amplitude responses are observed, allowing quantitative proximity evaluation for materials with similar triboelectric characteristics. At a fixed 50 mm separation, distinct responses were obtained for materials with different electronegativities (Figure 3g). Notably, the ITS detected a human target up to 1.1 m, with an output of ∼0.04 V at the maximum tested distance (Figure 3h). To evaluate the robustness of tele-perception, the effects of target approaching velocity and angle were investigated (Figure S15). Over velocities of 0.01−0.20 m s^{-1} at a fixed 20 mm displacement, the ITS maintained comparable voltage amplitudes, indicating limited velocity dependence within the tested range. In contrast, the output gradually decreased as the approaching angle varied from 0° to ±60° because of reduced electrostatic coupling. Despite this angle dependence, the ITS retained clear tele-perception responses across different approach directions, confirming its robustness for practical sensing applications. The 1.1 m measurement was obtained under ambient laboratory conditions at 25 °C and ∼38% RH. Because long-range electrostatic signals weaken with distance, humidity and nearby conductive objects may affect surface-charge retention and local electric-field distribution. Therefore, the reported 1.1 m distance represents the maximum tested human-target detection distance under the specified laboratory conditions. Collectively, these results demonstrate that microstructure-enhanced electric-field modulation, ionic-electronic coupling, and trap-assisted charge stabilization jointly enable sensitive and stable tele-perception before physical contact, providing a basis for subsequent material recognition and adaptive robotic interaction. Considering the environmental sensitivity of ionic migration, the effects of temperature and relative humidity on both haptic and tele-perception were evaluated (Figure S16). Both sensing modes showed relatively stable responses across the tested temperatures, whereas increasing humidity gradually reduced the output because of moisture-induced charge dissipation and weakened interfacial electrostatic coupling. The ITS is therefore primarily suited to indoor robotic perception under ambient conditions, while improving its adaptability to extreme environments remains an important direction for future work.

Precise perception and dexterous manipulation in unstructured environments remain as core challenges in embodied intelligence. Particularly when interacting with unknown objects of diverse materials and morphologies, the ability to infer physical attributes prior to contact and execute stable grasps is critical to task success.[52] To enhance robotic adaptability and interaction safety, a biomimetic bimodal perception system based on the ITS was developed, comprising a PVDF-$[SEt_3]NTf_2$-TiO_2 ternary composite film to integrate tele-perception with haptic perception. Leveraging the triboelectric effect, the system transduces electrostatic induction during an object approach and pressure variations upon contact into distinct electrical signatures. During the pre-contact stage, signal amplitude and polarity provide complementary cues regarding target proximity and triboelectric characteristics, which are subsequently combined with haptic information for material recognition and adaptive grasping. By incorporation of deep learning algorithms, these perception signals are decoded using the 1D-CNN to identify target properties, thereby enabling adaptive and intelligent grasping strategies.

As illustrated in Figure 4a, a self-powered biomimetic bimodal perception system was integrated into a robotic hand to establish a closed-loop framework, encompassing tele-perception → haptic perception → action feedback. During target approach and contact, distinct triboelectric signals were sequentially generated, enabling continuous spatiotemporal perception of object presence and interaction state. Because the signal characteristics differ before contact (tele-perception) and during contact (haptic perception), the same 1D-CNN architecture was independently trained for the two modalities as separate five-class classification tasks (Figure 4b). Five materials (nylon, paper, acrylic, Kapton, and PTFE) were evaluated. For each modality, 20 experimental groups were collected per material with 8 waveforms per group, yielding 160 samples per material and 800 samples per task. The two datasets were analyzed independently and split into training and held-out subsets at an 80:20 ratio using a fixed random state of 42. Through three convolutional blocks with hierarchical convolution and pooling, the model captured discriminative differences in signal amplitude, polarity, and waveform morphology arising from ionic-electronic regulation and TiO_2-assisted charge trapping (Figure 4c). Detailed preprocessing, network architecture, training parameters, and validation procedures are provided in Note S2 and Table S3. Each modality-specific 1D-CNN contains 215,685 trainable parameters, corresponding to ∼0.82 MB of 32-bit model weights, while global average pooling reduces memory requirements by avoiding a large fully connected feature layer. Hardware-specific inference latency and energy consumption were not measured because they depend strongly on the target computing platform and implementation. Therefore, no hardware-independent latency or energy-per-inference values are claimed. Nevertheless, the compact model size supports future embedded implementation. The model achieved 91.3% accuracy for material pre-recognition via tele-perception before contact and 90.28% for material recognition via haptic perception during contact (Figure 4d). Tele-perception classification signals were acquired at a fixed sensor-target separation of 50 mm. Building upon this perception capability, a closed-loop control strategy was further implemented (Figure 4e and Figure S18), enabling seamless transition from sensing to action. Entry of an object into the effective sensing range triggered an approach warning and prepared the robotic hand for grasping. Upon physical contact and signal exceeding a predefined threshold, a threshold-switching mechanism confirms object engagement and initiates grasp execution. Material-dependent control then adjusted grasping force and posture, using a high-threshold, high-force strategy for rigid objects and a low-threshold, compliant strategy for soft objects. Additional grasping demonstrations with objects of different sizes and geometries, including rectangular, spherical, cylindrical, and irregular shapes were performed to validate the practical adaptability, confirming successful tele-perception, haptic perception, and adaptive grasping (Movie S1). These results support robust perception to action manipulation beyond contact-only triggering. During these demonstrations, the robotic hand first detected object proximity through tele-perception, followed by haptic perception upon contact and adaptive grasp execution based on the acquired sensory information. These results demonstrate the feasibility of dynamic

Downloaded from pubs.acs.org/naletd/article-pdf/26/38/13053/6854065/acs.nanolett.6c03434.pdf by BEIJING INST PETROCHEMICAL TECHLGY user on 01 October 2026

https://doi.org/10.1021/acs.nanolett.6c03434
Nano Lett. 2026, 26, 13053−13062

perception to action manipulation under diverse object configurations and further support the potential of the ITS-based biomimetic bimodal perception system for practical robotic applications. A comparison with recently reported triboelectric and iontronic sensing systems is summarized in Table S4. Compared with existing platforms, the ITS uniquely integrates non-contact tele-perception and contact haptic sensing within a single self-powered device while providing AI-assisted material recognition and closed-loop robotic manipulation.

In conclusion, this work introduced iontronics into triboelectric sensing, transforming conventional electron-only, contact-triggered devices into multimodal systems integrating tele-perception and haptic perception. By establishing a synergistic ionic-electronic coupling mechanism within a PVDF-[SEt_3]NTf_2-TiO_2 ternary composite, we overcame the intrinsic limitations of pure electronic polarization. The integration of interfacial EDL reconstruction and TiO_2-assisted charge trapping stabilized the electrostatic field and suppressed charge dissipation. Optimized surface microstructuring further enhanced performance, yielding a peak open-circuit voltage of 124 V and a broad pressure detection range up to 70 kPa across three sensitivity regimes (S_1 = 1.13 V kPa^{-1}, S_2 = 4.48 V kPa^{-1}, and S_3 = 1.17 V kPa^{-1}), alongside human-target detection at distances of up to 1.1 m in the tele-perception mode. A 1D-CNN architecture effectively decoupled these bimodal signals, powering a biomimetic perception system that achieved material pre-recognition accuracy of 91.3% for tele-perception before contact and material recognition accuracy of 90.28% for haptic perception during contact. Leveraging these capabilities, a closed-loop control strategy dynamically adjusted grasping thresholds and modulated holding forces, effectively mitigating overload and slippage risks. This study transcends the spatiotemporal constraints of conventional single mode sensors, presenting a robust paradigm for autonomous robotics in unstructured environments relevant to precision manufacturing and advanced human−machine interaction.

■ ASSOCIATED CONTENT

Supporting Information

The Supporting Information is available free of charge at https://pubs.acs.org/doi/10.1021/acs.nanolett.6c03434.

Video of closed-loop robotic grasping of objects with varying sizes and geometries enabled by the ITS-based bimodal perception system (MP4)

Materials and Methods section; details of film fabrication, bimodal sensing mechanisms, COMSOL simulation, and 1D-CNN-based material classification; and supplementary figures and tables on material optimization, sensing performance, environmental stability, and robotic grasping demonstrations (PDF)

■ AUTHOR INFORMATION

Corresponding Authors

Zhong Lin Wang − *Beijing Institute of Nanoenergy and Nanosystems, Chinese Academy of Sciences, Beijing 101400, China*; Email: zlwang@binn.cas.cn

Di Wei − *Beijing Institute of Nanoenergy and Nanosystems, Chinese Academy of Sciences, Beijing 101400, China; Centre for Photonic Devices and Sensors, University of Cambridge, Cambridge CB3 0FA, UK;* orcid.org/0000-0003-2670-6362; Email: weidi@binn.cas.cn

Authors

Jiaxin Guo − *Beijing Institute of Nanoenergy and Nanosystems, Chinese Academy of Sciences, Beijing 101400, China; School of Nanoscience and Engineering, University of Chinese Academy of Sciences, Beijing 100049, China*

Yan Du − *Beijing Institute of Nanoenergy and Nanosystems, Chinese Academy of Sciences, Beijing 101400, China; School of Nanoscience and Engineering, University of Chinese Academy of Sciences, Beijing 100049, China;* orcid.org/0009-0007-2290-6873

Complete contact information is available at: https://pubs.acs.org/10.1021/acs.nanolett.6c03434

Author Contributions

#J.X.G. and Y.D. contributed equally to this work. D.W. and Z.L.W. proposed the idea and the project. D.W. supervised the whole project. J.X.G. and Y.D. designed all the experiments and carried out the experiments in this paper and analyzed the corresponding data. All the authors discussed the results and commented on the manuscript. D.W. and J.X.G. wrote this paper.

Notes

The authors declare no competing financial interest.

■ ACKNOWLEDGMENTS

This work was supported by the National Natural Science Foundation (Grant Number 22479016).

■ REFERENCES

(1) Wu, X.; Xie, Y.; Wu, Z.; Feng, Y.; Liang, Y.; Lu, L.; Yuan, W.; Yang, S.; Xing, D.; Zhong, Y.; et al. A bio-inspired proximity-tactile sensor array with beyond-extreme detection depth for embodied intelligence. *Int. J. Extreme Manuf.* **2026**, *8* (3), 035506.

(2) Xu, Q.; Zhang, B.; Cheung, Y. K.; Yang, Z.; Jiao, R.; Yao, S.; Hong, W.; Yu, H. A bio-inspired origami capacitive robotic e-skin with multimodal sensing capabilities. *npj Flexible Electron.* **2026**, *10* (1), 63.

(3) Laschi, C. The multifaceted approach to embodied intelligence in robotics. *Sci. Robot* **2025**, *10* (102), No. eadx2731.

(4) Li, S.; Xu, J. Multiaxis Force/Torque Sensor Technologies: Design Principles and Robotic Force Control Applications: A Review. *IEEE Sens. J.* **2025**, *25* (3), 4055−4069.

(5) Mao, Q.; Liao, Z.; Liu, S.; Yuan, J.; Zhu, R. An ultralight, tiny, flexible six-axis force/torque sensor enables dexterous fingertip manipulations. *Nat. Commun.* **2025**, *16* (1), 5693.

(6) Wang, J.; Chen, R.; Ji, D.; Xu, W.; Zhang, W.; Zhang, C.; Zhou, W.; Luo, T. Integrating In-Plane Thermoelectricity and Out-Plane Piezoresistivity for Fully Decoupled Temperature-Pressure Sensing. *Small* **2024**, *20* (12), 2307800.

(7) Cai, M.; Jiao, Z.; Nie, S.; Wang, C.; Zou, J.; Song, J. A multifunctional electronic skin based on patterned metal films for tactile sensing with a broad linear response range. *Sci. Adv.* **2021**, *7* (52), No. eabl8313.

(8) Zhang, J.; Yao, H.; Mo, J.; Chen, S.; Xie, Y.; Ma, S.; Chen, R.; Luo, T.; Ling, W.; Qin, L.; Wang, Z.; Zhou, W. Finger-inspired rigid-soft hybrid tactile sensor with superior sensitivity at high frequency. *Nat. Commun.* **2022**, *13* (1), 5076.

(9) Zhao, J.; Dai, S.; Wang, X.; Wang, Y.; Chen, Y.; Wu, G.; Chang, S.; Zhao, Z.; Liu, Z.; Zhang, H.; Xue, C.; Gao, L. PVDF-Based Piezoelectric Tactile Sensors: Advances in Material Design, Functional Optimization, and Applications. *Adv. Mater. Technol.* **2026**, *11* (9), e02194.

(10) Luo, Y.; Shao, J.; Chen, S.; Chen, X.; Tian, H.; Li, X.; Wang, L.; Wang, D.; Lu, B. Flexible Capacitive Pressure Sensor Enhanced by

Downloaded from pubs.acs.org/naletd/article-pdf/26/38/13053/6854065/acs.nanolett.6c03434.pdf by BEIJING INST PETROCHEMICAL TECHLGY user on 01 October 2026

Tilted Micropillar Arrays. *ACS Appl. Mater. Interfaces* **2019**, *11* (19), 17796−17803.
(11) Uzabakiriho, P. C.; Wang, M.; Ma, C.; Zhao, G. Stretchable, breathable, and highly sensitive capacitive and self-powered electronic skin based on core-shell nanofibers. *Nanoscale* **2022**, *14* (17), 6600−6611.
(12) Hu, J.; Cao, D.; Li, Y.; Liu, H. Polymer-Based Optical Waveguide Tactile Sensing Method for 3-D Surfaces. *IEEE Sens. J.* **2023**, *23* (8), 8761−8768.
(13) Pu, M.; Zhao, T.; Zhang, L.; Han, C.; Chai, Z.; Zhou, Y.; Ding, H.; Wu, Z. An AI-Enabled All-In-One Visual, Proximity, and Tactile Perception Multimodal Sensor. *Adv. Robot. Res.* **2025**, 202500062.
(14) Cho, I. J.; Lee, H. K.; Chang, S. I.; Yoon, E. Compliant Ultrasound Proximity Sensor for the Safe Operation of Human Friendly Robots Integrated with Tactile Sensing Capability. *J. ELECTR ENG TECHNOL* **2017**, *12* (1), 310−316.
(15) Liu, T.-T.; Zhu, Y.-H.; Shu, J.-C.; Zhang, M.; Cao, M.-S. Patterned MXene-enabled switchable health monitoring and electromagnetic protection for architecture. *Mater. Today Phys.* **2023**, *31*, 100988.
(16) Ge, J.; Wang, X.; Drack, M.; Volkov, O.; Liang, M.; Canon Bermudez, G. S.; Illing, R.; Wang, C.; Zhou, S.; Fassbender, J.; Kaltenbrunner, M.; Makarov, D. A bimodal soft electronic skin for tactile and touchless interaction in real time. *Nat. Commun.* **2019**, *10* (1), 4405.
(17) Li, N.; Liu, L.; Liu, Y.; Leng, J. Metamaterial-Based Electronic Skin with Conformality and Multisensory Integration. *Adv. Funct. Mater.* **2024**, *34* (49), 2406789.
(18) Wu, B.; Jiang, T.; Yu, Z.; Zhou, Q.; Jiao, J.; Jin, M. L. Proximity Sensing Electronic Skin: Principles, Characteristics, and Applications. *Adv. Sci.* **2024**, *11* (13), 2308560.
(19) Haider, Z.; Haleem, A.; Ahmad, R. u. S.; Farooq, U.; Shi, L.; Claver, U. P.; Memon, K.; Fareed, A.; Khan, I.; Mbogba, M. K.; et al. Highly porous polymer cryogel based tribopositive material for high performance triboelectric nanogenerators. *Nano Energy* **2020**, *68*, 104294.
(20) Dong, K.; Peng, X.; Wang, Z. L. Fiber/Fabric-Based Piezoelectric and Triboelectric Nanogenerators for Flexible/Stretchable and Wearable Electronics and Artificial Intelligence. *Adv. Mater.* **2020**, *32* (5), 1902549.
(21) Lin, Z.; Deng, Y.; Deng, L.; Zou, M.; Lu, Y.; Gao, H.; Chen, J.; Xu, F.; Guo, H. Triboelectric Nanogenerator-Enabled Wireless Self-Powered Sensing System Leveraging Radio Frequency. *SmartSys* **2026**, *2* (2), No. e70031.
(22) Sohel Rana, S. M.; Faruk, O.; Selim Reza, M.; Robiul Islam, M.; Kim, H.; Yeong Park, J. All porous Ecoflex and SEBS-based stretchable high-performance triboelectric nanogenerator for self-powered human activity monitoring. *Chem. Eng. J.* **2024**, *488*, 151050.
(23) Rana, S. M. S.; Wang, Z. L. Recent advances and prospective strategies for improving the performance of triboelectric nanogenerators. *Coord. Chem. Rev.* **2025**, *543*, 216914.
(24) Rana, S. M. S.; Rahman, M. T.; Salauddin, M.; Sharma, S.; Maharjan, P.; Bhatta, T.; Cho, H.; Park, C.; Park, J. Y. Electrospun PVDF-TrFE/MXene Nanofiber Mat-Based Triboelectric Nanogenerator for Smart Home Appliances. *ACS Appl. Mater. Interfaces* **2021**, *13* (4), 4955−4967.
(25) Du, Y.; Shen, P.; Liu, H.; Zhang, Y.; Jia, L.; Pu, X.; Yang, F.; Ren, T.; Chu, D.; Wang, Z.; Wei, D. Multi-receptor skin with highly sensitive tele-perception somatosensory. *Sci. Adv.* **2024**, *10* (37), No. eadp8681.
(26) Yuan, F.; Liu, S.; Zhou, J.; Wang, S.; Wang, Y.; Xuan, S.; Gong, X. Smart touchless triboelectric nanogenerator towards safeguard and 3D morphological awareness. *Nano Energy* **2021**, *86*, 106071.
(27) Du, Y.; Shen, P.; Liu, H.; Zhang, Z.; Yang, F.; Chu, D.; Ren, T.; Wang, Z. L.; Wei, D. Meta-structured electret heterointerface for resilient and adaptive tele-perception in embodied intelligence. *Matter* **2025**, *8* (12), 102363.
(28) Ahmad, R. u S.; Haleem, A.; Haider, Z.; Claver, U. P.; Fareed, A.; Khan, I.; Mbogba, M. K.; Memon, K.; Ali, W.; He, W.; Hu, P.; Zhao, G. Realizing the Capability of Negatively Charged Graphene Oxide in the Presence of Conducting Polyaniline for Performance Enhancement of Tribopositive Material of Triboelectric Nanogenerator. *Adv. Electron. Mater.* **2020**, *6* (5), 2000034.
(29) Salauddin, M.; Rana, S. M. S.; Sharifuzzaman, M.; Lee, S. H.; Zahed, M. A.; Do Shin, Y.; Seonu, S.; Song, H. S.; Bhatta, T.; Park, J. Y. Laser-carbonized MXene/ZiF-67 nanocomposite as an intermediate layer for boosting the output performance of fabric-based triboelectric nanogenerator. *Nano Energy* **2022**, *100*, 107462.
(30) Fan, F.-R.; Lin, L.; Zhu, G.; Wu, W.; Zhang, R.; Wang, Z. L. Transparent Triboelectric Nanogenerators and Self-Powered Pressure Sensors Based on Micropatterned Plastic Films. *Nano Lett.* **2012**, *12* (6), 3109−3114.
(31) Pradel, K. C.; Fukata, N. Systematic optimization of triboelectric nanogenerator performance through surface micropatterning. *Nano Energy* **2021**, *83*, 105856.
(32) Du, Y.; Chu, D.; Amaratunga, G.; Wei, D. Triboelectric Tactile Sensors for Intelligent Systems. *SmartSys* **2026**, *2* (2), No. e70023.
(33) Shi, K.; Chai, B.; Zou, H.; Min, D.; Li, S.; Jiang, P.; Huang, X. Dielectric Manipulated Charge Dynamics in Contact Electrification. *Research* **2022**, *2022*, 9862980.
(34) Kim, M. P.; Um, D.-S.; Shin, Y.-E.; Ko, H. High-Performance Triboelectric Devices via Dielectric Polarization: A Review. *Nanoscale Res. Lett.* **2021**, *16* (1), 35.
(35) Zhang, N.; He, Y.; Wang, L. Designing iontronic pressure sensors: a perspective from multiscale mechanics. *Iontronics* **2025**, *1* (1), 5.
(36) Han, J. H.; Moon, H. C. Monolithically integrated ionic triboelectric nanogenerators for deformable energy harvesting and self powered sensing. *npj Flexible Electron.* **2025**, *9* (1), 114.
(37) Fan, K.; Li, K.; Wang, Z.; Men, W.; Wu, X.; Cheng, J.; Zhang, J. An unprecedented strategy with electric double layer and adaptive ionic liquid in fully ionogel fiber-based TENG for enhanced output and dynamic stability. *Nano Energy* **2025**, *135*, 110658.
(38) Wang, X.; Guo, C.; Su, Z.; Zhou, L.; Xu, D.; Zhang, R.; Teng, B.; Bai, N.; Wang, W. Flexible iontronic pressure sensing technology: advanced structural ionic layer. *Iontronics* **2026**, *2* (1), 1.
(39) Aazem, I.; Kumar, C.; Walden, R.; Babu, A.; Goswami, A.; Hinder, S. J.; Khandelwal, G.; Mulvihill, D. M.; Mcgranaghan, G.; Pillai, S. C. Electroactive phase dependent triboelectric nanogenerator performance of PVDF-TiO_2 composites. *Energy Adv.* **2025**, *4* (5), 683.
(40) Chen, X.; Liu, Y.; Sun, Y.; Zhao, T.; Zhao, C.; Khattab, T. A.; Lim, E. G.; Sun, X.; Wen, Z. Electron trapping & blocking effect enabled by MXene/TiO_2 intermediate layer for charge regulation of triboelectric nanogenerators. *Nano Energy* **2022**, *98*, 107236.
(41) Wang, N.; Liu, Y.; Feng, Y.; Yang, J.; Wu, Y.; Zhang, B.; Li, Y.; Li, B.; Wang, S.; Ye, E.; Zhang, Y.-W.; Loh, X. J.; Zhou, F.; Li, Z.; Wang, D. Revamping Triboelectric Output by Deep Trap Construction. *Adv. Mater.* **2024**, *36* (13), 2303389.
(42) Li, G.; Li, L.; Zhang, P.; Chang, C.; Xu, F.; Pu, X. Ultrastretchable and healable hydrogel-based triboelectric nanogenerators for energy harvesting and self-powered sensing. *RSC Adv.* **2021**, *11* (28), 17437−17444.
(43) Pu, X.; Liu, M.; Chen, X.; Sun, J.; Du, C.; Zhang, Y.; Zhai, J.; Hu, W.; Wang, Z. L. Ultrastretchable, transparent triboelectric nanogenerator as electronic skin for biomechanical energy harvesting and tactile sensing. *Sci. Adv.* **2017**, *3* (5), No. e1700015.
(44) Du, G.; Shao, Y.; Luo, B.; Liu, T.; Zhao, J.; Qin, Y.; Wang, J.; Zhang, S.; Chi, M.; Gao, C.; Liu, Y.; Cai, C.; Wang, S.; Nie, S. Compliant Iontronic Triboelectric Gels with Phase-Locked Structure Enabled by Competitive Hydrogen Bonding. *Nano-Micro Lett.* **2024**, *16* (1), 170.
(45) Lv, H.; Wang, Z.; Gao, Z.; Song, H. Highly stretchable, self-healable, and environment-adaptable ionogel-based high-output triboelectric nanogenerator for self-powered wearable ionotronics. *Chem. Eng. J.* **2025**, *509*, 161247.
(46) Kim, J. S.; Lee, S. C.; Hwang, J.; Lee, E.; Cho, K.; Kim, S.-J.; Kim, D. H.; Lee, W. H. Enhanced Sensitivity of Iontronic Graphene

Downloaded from pubs.acs.org/naletd/article-pdf/26/38/13053/6854065/acs.nanolett.6c03434.pdf by BEIJING INST PETROCHEMICAL TECHLGY user on 01 October 2026

https://doi.org/10.1021/acs.nanolett.6c03434
Nano Lett. 2026, 26, 13053−13062

Tactile Sensors Facilitated by Spreading of Ionic Liquid Pinned on Graphene Grid. *Adv. Funct. Mater.* **2020**, *30* (14), 1908993.
(47) Qin, S.; Yang, P.; Liu, Z.; Hu, J.; Li, N.; Ding, L.; Chen, X. Triboelectric sensor with ultra-wide linear range based on water-containing elastomer and ion-rich interface. *Nat. Commun.* **2024**, *15* (1), 10640.
(48) Wang, B.; Zhao, H.; Jin, C.; Xu, Y.; Ding, W. Ionic-electrostatic modeling of solid-liquid triboelectric nanogenerators. *Iontronics* **2026**, *2* (2), 17.
(49) Harnchana, V.; Ngoc, H. V.; He, W.; Rasheed, A.; Park, H.; Amornkitbamrung, V.; Kang, D. J. Enhanced Power Output of a Triboelectric Nanogenerator using Poly(dimethylsiloxane) Modified with Graphene Oxide and Sodium Dodecyl Sulfate. *ACS Appl. Mater. Interfaces* **2018**, *10* (30), 25263−25272.
(50) Fernandes, L. C.; Pereira, N.; Peřinka, N.; Botelho, G.; Correia, D. M.; Lanceros-Mendez, S. Flexoionic Effect on Ionic Liquid Based Polymer Composites for Bending and Pressure Sensing Applications. *Adv. Mater. Technol.* **2025**, *10* (17), No. e00465.
(51) Kumar, A. D.; Arunachalam, N.; Jayaganthan, R. Self-poled Ag nanowire/ionic liquid-infused PVDF nanocomposites for enhanced triboelectric performance via additive manufacturing. *Compos. Part B-Eng* **2025**, *303*, 112604.
(52) Li, L.; Sun, H.; Wang, J.; Guo, Z. H.; Pu, X.; Sun, F. The Next Chapter of Human-Like Tactile Perception: Neural Decoding to Embodied Intelligence. *SmartSys* **2026**, *2* (2), No. E70024.

Downloaded from pubs.acs.org/naletd/article-pdf/26/38/13053/6854065/acs.nanolett.6c03434.pdf by BEIJING INST PETROCHEMICAL TECHLGY user on 01 October 2026

https://doi.org/10.1021/acs.nanolett.6c03434
Nano Lett. 2026, 26, 13053−13062